Development of a Multidirectional Controlled Small-Scale Spherical MR Actuator for Haptic Applications

Dapeng Chen , *Student Member, IEEE*, Aiguo Song , *Senior Member, IEEE*, Lei Tian,
Qiangqiang Ouyang, and Pengwen Xiong

***Abstract*—In robotics and haptics, actuators that move at multiple degrees of freedom (DOFs) without the intermediate transmission mechanisms and have high force/torque output with compact size are widely expected to improve the stability and transparency of interactions. For this reason, utilizing the characteristics that the rheological properties of magnetorheological (MR) fluid can be continuously and reversibly changed by an external magnetic field within a few milliseconds, a multidirectional controlled three-DOF spherical MR actuator is proposed in this paper. Through the special design of the stator part, the actuator can implement force feedback control in multiple directions. Then, based on the calculated torque model and analysis of the magnetic circuit, finite-element analysis is used to optimize the geometry and internal magnetic field distribution of the actuator. In order to achieve precise control and positioning of multi-DOF motion, a small inertial measurement unit is integrated in the upper part of the joystick. We built a prototype of this actuator and tested its performance under various control conditions. The results show that the actuator can provide force feedback with reasonable magnitude and direction to users according to the change of interaction conditions, thus overcoming the disadvantage of the existing spherical MR actuators that limit the movement of the user in all directions after being activated.**

***Index Terms*—Force feedback, magnetorheological (MR) fluid, multidirectional control, multiple-degree-of-freedom (multi-DOF) motion, spherical actuator.**

D. Chen, A. Song, and Q. Ouyang are with the State Key Laboratory of Bioelectronics, Jiangsu Key Laboratory of Remote Measurement and Control, School of Instrument Science and Engineering, Southeast University, Nanjing 210096, China (e-mail: 230149546@seu.edu.cn; a.g.song@seu.edu.cn; 230169559@seu.edu.cn).

L. Tian is with the School of Automation, Nanjing Institute of Technology, Nanjing 211167, China (e-mail: tianleinjit@163.com).

P. Xiong is with the School of Information Engineering, Nanchang University, Nanchang 330031, China (e-mail: steven.xpw@ncu.edu.cn).

Color versions of one or more of the figures in this paper are available online at http://ieeexplore.ieee.org.

I. INTRODUCTION

IN THE field of human–computer interaction (HCI), haptic devices are becoming more and more valued because they are capable of simulating the interaction between an operator and virtual or distant objects and transmitting the information generated during the interaction to the operator through appropriate haptic feedback [1]. Nowadays, many haptic devices have been developed and widely used in virtual reality [2], teleoperation [3], medical [4], and other applications. An ideal haptic device should be able to convey interactive information to users with high fidelity through force feedback or tactile feedback, while taking into consideration both transparency and stability [5]. In the design of haptic devices, the actuator's power, volume, weight, inertia, friction, etc., are often the key considerations. However, the degree of freedom (DOF) is also an important design parameter.

Common haptic devices typically employ one-DOF actuators that are capable of rotational or linear motion, such as active actuators based on motors [6], or semiactive actuators based on electrorheological (ER) fluid [7] or magnetorheological (MR) fluid [8]–[11] to achieve force feedback. For multi-DOF operation tasks, traditional haptic devices are often driven by plural one-DOF actuators through series or parallel mechanisms [12]–[15]. However, a large number of transmission mechanisms, such as connecting rods, gears, and worms, inevitably increase the mass, volume, friction, backlash, and singularities in the operating space of the device. These disadvantages result in the traditional haptic devices being unable to be well suited for applications such as wearable or exoskeletal devices, which have limited device weight or operating space.

With respect to multi-DOF haptic devices, spherical actuators that are able to naturally perform three-DOF rotational motion in a single joint are promising alternatives to conventional haptic devices. The spherical actuator is mainly composed of a stator and a spherical rotor, which reduces the volume and structural complexity of the multi-DOF haptic device, and eliminates the singularities in the working space and overcomes the disadvantages of the series or parallel structure [16]. According to the nature of force/torque reflection, spherical actuators can be classified into active and passive types. At present, most active spherical actuators are driven by electromagnetic forces [16]–[18]. This type of actuator has a similar working

principle as the motor. Although it can be operated in three DOFs, it is still considered as an extension of the one-DOF rotary motor in terms of structure. Besides, since they cannot be used in conjunction with gearboxes, and spherical rotors need to be specially designed, these active spherical actuators inevitably have disadvantages such as low torque-to-volume ratio, high inertia, and complicated structure.

In recent years, various multi-DOF spherical semiactive actuators based on smart materials, such as MR fluid and ER fluid, have been studied and developed to provide passive force feedback. MR fluid and ER fluid are very promising smart materials, and they are usually present in liquid form [19]. By controlling the magnetic field applied to the MR fluid or the electric field applied to the ER fluid, their rheological properties can be changed rapidly and reversibly, enabling continuous control of the working conditions. The semiactive actuator can only produce passive force feedback, and it will not input energy to the controlled system during operation, so there is no risk of causing the controlled system to be unstable or harming the operator. At the same time, they can adjust their own dynamic characteristics according to the state change of the controlled object, so as to track and realize the optimal state response to the controlled object in real time. Smart material-based semiactive actuators have the advantages of active and passive actuators at the same time and have significant advantages of low energy consumption, low inertia, compact structure, and intrinsically safe and stable. For example, Bose and Berkemeier [20] first introduced an ER-fluid-based spherical haptic device. The device had a rotor diameter of 100 mm and produced a resistance torque of 1.2 N·m under the control of 2.8-kV/mm field strength. Han and Choi [21] designed a display device capable of generating two-DOF force feedback by integrating an ER-fluid-based spherical joint and four ac motors placed at 90° intervals. The ER joint was manufactured utilizing clutch and spherical electrode mechanisms and had an operating range from 0.84 to 1.5 rad. However, this device is bulky, and since the shear stress of the ER fluid is small, the ER joint produces only 1.08-N resistance force. Later, Oh et al. [22] developed an ER-fluid-based four-DOF haptic master device for minimally invasive surgery. The device was composed of an ER spherical joint for three-DOF rotational movement and an ER piston device for one-DOF translational movement. The ER spherical joint was made of an 84-mm-diameter metal sphere and had a maximum repulsive torque of 0.775 N·m. However, due to the lower maximum yield strength of the ER fluid, ER-fluid-based spherical actuators generally need to have a large volume. In addition, the operating voltage of ER actuators up to several kilovolts is potentially dangerous to operators.

Compared with the ER fluid, the maximum yield strength of the MR fluid can reach nearly 20 times that of the ER fluid, and the voltage required to activate the magnetic field is small. Therefore, a spherical actuator developed based on MR fluid significantly increases the force/torque–volume ratio, which is critical to achieving miniaturization of haptic devices. Senkal and Gurocak [23] explored a three-DOF MR spherical brake designed by the serpentine flux path approach and utilized an optical position measurement system to measure the orientation of the sphere movement. A prototype brake was manufactured by a high-permeability metal sphere with 76.2-mm diameter and generated a maximum resistance torque of 3.7 N·m. Once the coil is activated, the brake is able to provide force feedback in three DOFs at the same time. In addition, Telleria et al. [24] also proposed a spherical joint based on MR fluid for precise orientation control. The interior of the joint includes a permanent magnet and a coil. By controlling the current in the coil, the magnetic flux density applied to the MR fluid and the motion direction of the ball can be dynamically changed.

As mentioned earlier, although there are some three-DOF passive spherical actuators, one of their common problems is that when activated, the actuator locks all three-DOF motions simultaneously, which restricts motion of the user in all directions. For example, once pierced into a virtual wall, the fixed-size force feedback generated by the MR/ER actuator will cause difficulties for the user to move within the virtual wall or slide on the virtual wall surface, which will affect the user's perception and judgment of the properties of the virtual object. Second, if only semiactive actuators are used for virtual wall operations, the user will feel "stuck in the wall" when pulling a haptic interaction point (HIP) back from the virtual wall [25]. The usual solution is to combine the semiactive actuator with a dc motor to perform force feedback [25] or to add a force sensor to the force feedback system [22], [23]. However, dc motors do not integrate well with spherical semiactive actuators, and force sensors are considerably expensive and increase system complexity. In addition, existing spherical haptic devices generally have a large volume, and the resulting increase in weight and power consumption is not conducive to integrating these devices with portable devices or as key components in complex machines.

Being able to provide users with force feedback that varies with the interaction environment in different DOFs and directions is one of the main goals of developing multi-DOF actuators. In this paper, we developed a multidirectional controlled three-DOF spherical actuator based on MR fluid. The actuator has a specially designed stator that replaces the traditional magnetic field controlled by a single coil with eight separate coils and magnetic circuits. Through the individual control of each magnetic circuit, the actuator can be made to output variable passive force/torque in different directions and DOFs. Next, the MPU 6050-based inertial measurement unit (IMU) is integrated in the actuator's joystick so that the proposed MR actuator can correctly output the force/torque according to the change of the interaction direction. The data fusion algorithm based on the Kalman filter is used to correct and estimate the attitude of the joystick. Finally, we tested the physical characteristics of the MR actuator, such as output torque and transient response, and evaluated its actual application performance through softness display and friction display experiments.

II. DESIGN OF THE SPHERICAL MR ACTUATOR

A. Structure Design

The spherical MR actuator is usually operated in shear mode and consists of the spherical rotor, stator, coil, and MR fluid filled in the gap between the rotor and the stator. The rotor and the stator are generally made of ferromagnetic materials with
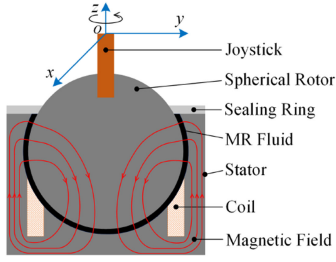
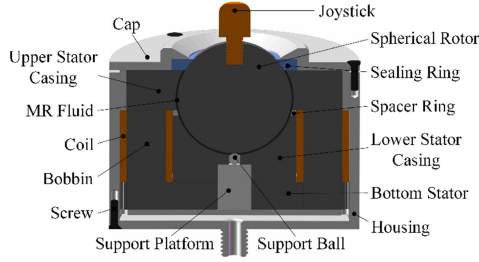Fig. 1. Working principle of the conventional spherical MR actuator.

Fig. 2. Schematic of the proposed multidirectional controlled spherical MR actuator.
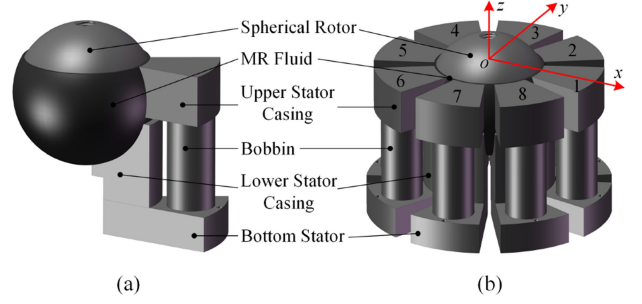

(a)   (b)

Fig. 3. Magnetic circuit composition of the spherical MR actuator. (a) Components passed by a complete magnetic circuit. (b) Structural distribution of eight independent magnetic circuits in the actuator.
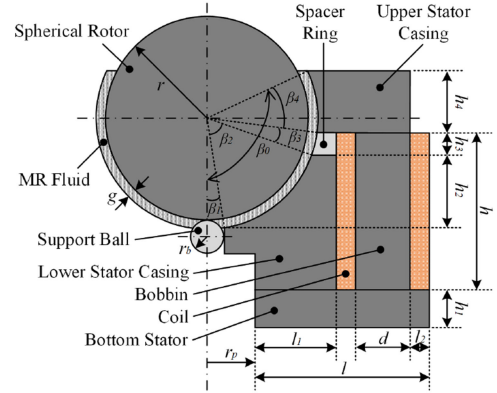

Fig. 4. Simplified structural scheme of the complete magnetic circuit geometry.

a high magnetic permeability. The coil is made of enameled copper wire wound inside the stator. When a current is applied to the coil, a magnetic field is generated, and magnetic flux lines will pass through the spherical rotor, the MR fluid, and the stator to form closed magnetic circuits. Fig. 1 depicts the structure and magnetic circuits of a simplified conventional spherical MR actuator. After the coil is energized, the user engages the pitching, rolling, and yawing movements with the joystick to simultaneously sense force feedback in three DOFs.

To achieve the control of forces in different interaction directions, in this paper, the stator is divided into eight parts on average and separated from each other with a nonmagnetic material to reduce the interference between different magnetic fields. Fig. 2 shows a schematic of the multidirectional controlled spherical MR actuator. The actuator is mainly composed of the joystick, cap, spherical rotor, sealing ring, MR fluid, upper stator casing, spacer ring, bobbin, coil, lower stator casing, bottom stator, housing, and support platform. Among them, the yokes composed of the spherical rotor, upper stator casing, bobbin, lower stator casing, and bottom stator are all made of electromagnetic pure iron (DT4) with high magnetic permeability to form magnetic circuits. The cap, spacer ring, and housing are made of aluminum alloys with low magnetic permeability to reduce the magnetic flux leakage and the weight of the actuator. The other parts are made of nonmagnetic material. The joystick is screwed to the spherical rotor. The seal ring and the support ball serve to determine the relative position between the spherical rotor and the stator. The MR fluid fills the gap between the rotor and the stator. The spacer ring is sandwiched between the upper and lower stator casings and serves to adjust the magnetic flux path. Due to the requirement for independent force/torque control in eight directions, the actuator contains eight coils and bobbins. Fig. 3 shows the magnetic circuit composition of the MR actuator.

Fig. 4 shows a simplified structural scheme of the complete magnetic circuit geometry in the chosen actuator. We denote by r the radius of the spherical rotor, g the height of the MR fluid filled between the rotor and the stator, r_b the radius of the support ball, and r_p the radius of the support platform. The heights of the bottom stator, the curved part of the lower stator casing, the spacer ring, and the upper stator casing are denoted by h_1, h_2, h_3, and h_4, respectively. The diameter and height of the bobbin are d and h, respectively, and the thickness of the coil is l_2. The central angles corresponding to the arc portions of the lower stator casing, the spacer ring, and the upper stator casing are β_2, β_3, and β_4, respectively.

In Fig. 4, according to the magnetic flux conservation law of the magnetic circuit $\Phi = BA$, magnetic fluxes passing through the upper and lower stator casing are equal. In order to obtain the ideal force feedback effect, it is necessary to ensure the uniformity of the magnetic flux density applied to the MR fluid [23]. Therefore, the surface area of the curved part of the upper and lower stator casing should be equal, and the following equation can be obtained:

$$\int_{\beta_1}^{\beta_1+\beta_2} \int_0^{\alpha_0} (r+g)^2 \sin\beta \, d\alpha d\beta$$
$$= \int_{\beta_1+\beta_2+\beta_3}^{\beta_0} \int_0^{\alpha_0} (r+g)^2 \sin\beta \, d\alpha d\beta \Rightarrow$$
$$\cos(\beta_1+\beta_2) + \cos(\beta_1+\beta_2+\beta_3) - \cos(\beta_0) = \cos\beta_1. \tag{1}$$

From Fig. 4, we can also know

$$\sin \beta_1 = \frac{r_b}{r+g} \tag{2}$$

$$\beta_1+\beta_2+\beta_3+\beta_4 = \beta_0 \tag{3}$$

$$h_2 = (r+g)(\cos \beta_1 - \cos(\beta_1 + \beta_2)) \tag{4}$$

$$h_3 = (r+g)(\cos(\beta_1 + \beta_2) - \cos(\beta_1 + \beta_2 + \beta_3)) \tag{5}$$

$$h_4 = (r+g)(\cos(\beta_1 + \beta_2 + \beta_3) + \sin(\beta_0 - \frac{\pi}{2})). \tag{6}$$

B. Torque Model

The key to the force feedback of the spherical actuator is the control of the working state of the MR fluid. MR fluid is a suspension mixture formed by adding ferromagnetic easy-to-magnetize solid particles and stabilizers to a nonmagnetic carrier fluid [26]. When a magnetic field acts on the MR fluid, the ferromagnetic particles randomly scattered in the carrier liquid are magnetized, and a plurality of chain or columnar fiber structures arranged in the direction of the magnetic field are rapidly formed between the two plates [27]. As the strength of the magnetic field increases, these fiber structures increase and thicken, increasing the viscosity and shear yield strength of the MR fluid. The relative movement of the two plates occurs only when the external force is so large that the formed fiber structures can be cut.

According to the field-dependent properties, the yield stress of MR fluid can be described by the Bingham plastic model, which has been proved by many studies to be an effective and simple model for designing MR actuators [26]. In this model, the shear stress τ of the MR fluid flowing under steady shear conditions is managed by the Bingham equation [27]

$$\tau = \tau_y(B)\text{sgn}(\dot{\gamma}) + \eta\dot{\gamma} \tag{7}$$

where $\tau_y(B)$ is the dynamic yield stress of the MR fluid caused by the magnetic flux density B, and it could be obtained from the specifications of the given MR fluid. η is the field-independent plastic viscosity, and $\dot{\gamma}$ is the shear rate. Therefore, the output torque T_{out} generated by the spherical MR actuator includes the field-dependent controllable torque T_τ, the viscous torque T_η, and the mechanical friction torque T_f, which can be expressed as

$$
\begin{aligned}
T_{\text{out}} &= T_\tau + T_\eta + T_f \\
T_\tau &= \int_A r_{\text{arm}}\tau_y(B)\,\text{d}A \\
T_\eta &= \int_A r_{\text{arm}}\eta\dot{\gamma}\,\text{d}A
\end{aligned}
\tag{8}
$$

where A denotes the surface area of the sphere that is activated by the magnetic field; r_{arm} is the moment arm, that is, the distance from the point on the surface of the sphere to the axis of rotation. In actual haptic applications, the rotational speed of the MR actuator is slower, so the T_η, which is proportional to the angular velocity, is small and can be ignored. Similarly, we also ignore T_f in our calculations.

When the rotor is rotating, the maximum torque of the MR actuator on the three axes needs to be calculated separately. Fig. 5 shows a spherical coordinate system for torque modeling. The position of any point on the sphere surface is described by
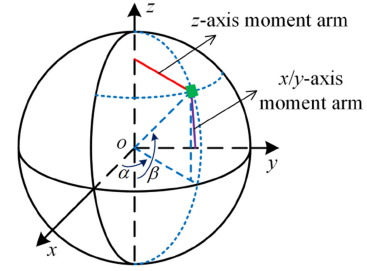

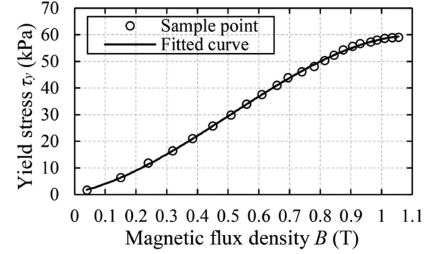Fig. 5.   Spherical coordinate system for torque modeling.

Fig. 6.   Yield stress–B relationship of MRF-140CG.

the rotation angles α and β. The moment arm of the spherical rotor on three axes can be expressed as

$$r_{\text{arm}}^z = r \sin \beta \tag{9}$$

$$r_{\text{arm}}^x = r_{\text{arm}}^y = r\sqrt{(\cos \beta)^2 + (\sin \alpha \cdot \sin \beta)^2}. \tag{10}$$

According to (8) and (9), the output torque for the z-axis in yawing motion is derived as

$$
\begin{aligned}
T_{\text{out}}^z \approx T_\tau^z &= \int_0^{\beta_0}\int_0^{\alpha_0} \tau_y r^3 (\sin\beta)^2 \,d\alpha d\beta \\
&= \tau_y r^3 \alpha_0 \left(\frac{\beta_0}{2} - \frac{\sin 2\beta_0}{4} \right)
\end{aligned}
\tag{11}
$$

where α_0 and β_0 are both constant angles of the stator. Similarly, using (8) and (10), the x/y-axis output torque in pitching/rolling motion is

$$
\begin{aligned}
T_{\text{out}}^x = T_{\text{out}}^y \approx T_\tau^x &= T_\tau^z(\beta_0 = \pi) - \\
\int_0^{\pi - \beta_0}\int_0^{\alpha_0} &\tau_y r^3 \sin\beta\sqrt{(\cos\beta)^2 + (\sin\alpha\sin\beta)^2}\,d\alpha d\beta.
\end{aligned}
\tag{12}
$$

According to (11) and (12), it can be seen that increasing the yield stress of the MR fluid significantly increases the output torque of the MR actuator. For this reason, the MR fluid employed is MRF-140CG from Lord Corporation, which has a very large saturation yield strength, and the relationship between its yield stress and magnetic flux density is shown in Fig. 6. With the increase of magnetic flux density, the yield stress of MR fluid increases approximately linearly and tends to saturate when the magnetic flux density reaches 1 T. An approximate polynomial of the dynamic yield stress $\tau_y(B)$ can be obtained by the least-squares curve-fitting method, which is expressed as

$$\tau_y(B) = -66.434B^3 + 99.911B^2 + 24.188B + 0.6812. \tag{13}$$

In this paper, the central angle corresponding to each independent magnetic circuit unit in the stator is $35°$, and the central

angle corresponding to the spacer between two magnetic circuit units is 10°. Taking yawing motion as an example, when a single magnetic circuit unit is activated, $\alpha_0 = 35\pi/180$ rad. When eight magnetic circuit units are activated at the same time, $\alpha_0 = 280\pi/180$ rad. In addition, we set the maximum value of β_0 to $120\pi/180$ rad in order to provide sufficient motion space for the joystick.

C. Magnetic Field Analysis

In addition to the design of the mechanical structure, the electromagnetic properties also have a significant influence on the performance of the proposed MR actuator [28]. To effectively apply the magnetic field to the MR fluid, a single magnetic circuit unit needs to be electromagnetically designed. The magnetic field in the magnetic circuit is generated by applying a current I to the coil with N turns. According to Ampere's law, the relationship between the magnetomotive force F of the magnetic circuit and the corresponding magnetic field strength can be obtained as

$$F = NI = H_y l_y + H_m l_m \qquad (14)$$

where H is the magnetic field strength and l is the length of the magnetic flux path. The subscripts y and m represent the physical properties corresponding to the yoke and the MR fluid, respectively. The length of the magnetic flux path in the MR fluid has been set to $l_m = g$, and DT4 is employed to manufacture the rotor and stator, so H_y is also determined. Under a certain magnetomotive force, the method of increasing the magnetic field utilization of the MR fluid is to minimize the length of the magnetic flux path in the yoke. According to the B–H relationship of the materials used in the magnetic circuit ($B = \mu_0 \mu_k H$, μ_0 is the permeability of the vacuum, and μ_k is the relative permeability of the material), and in combination with $\Phi = BA$, (14) can be expressed as

$$F = NI = \frac{B_y l_y}{\mu_0 \mu_y} + \frac{B_m l_m}{\mu_0 \mu_m} = \frac{\Phi l_y}{\mu_0 \mu_y A_y} + \frac{\Phi l_m}{\mu_0 \mu_m A_m}. \qquad (15)$$

Then, the reluctance in the yoke and the MR fluid can be defined as

$$R_y = \frac{l_y}{\mu_0 \mu_y A_y}, R_m = \frac{l_m}{\mu_0 \mu_m A_m}. \qquad (16)$$

Equation (16) illustrates $l_y \propto R_y$. One of the important design metrics of an MR actuator is the response time. Generally, an ideal MR actuator should have a fast response time. Although it takes only a few milliseconds to change the rheological properties of the MR fluid, the time constant of the magnetic circuit is determined by the MR fluid and the yoke. The time constant of the yoke is $t_y = L_y/R_y \propto 1/(R_y)^2$ [28]. Therefore, decreasing the R_y will increase the response time of the MR actuator. From (16), the method of increasing R_y is to reduce the cross-sectional area A_y of the yoke.

Fig. 7 shows the B–H curve of DT4 used for manufacturing the yoke, and it can be seen that when the magnetic flux density applied to the yoke is greater than 1.6 T, the magnetic field intensity sharply increases. From (14), under a certain magnetomotive force, an increase of the magnetic field strength in the yoke will result in a decrease of the magnetic field strength
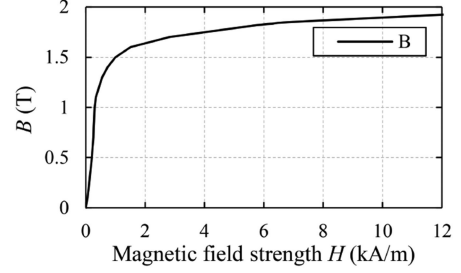

Fig. 7. B–H curve of DT4.

applied to the MR fluid, which is contrary to the design principle. Therefore, A_y cannot be reduced without limitation. According to the magnetic flux conservation rule, when the magnetic flux density of the component in the yoke reaches 1.6 T, the corresponding cross-sectional area is the minimum A_y that the component can take.

D. Optimization and Finite-Element Analysis

Generally, three main factors need to be considered when designing an MR actuator, namely, structural design, excitation design, and dynamic characteristics. In order to design a high-performance MR actuator, we use the finite-element method to optimize the structure of the actuator. Since the geometry of a single magnetic circuit unit in the MR actuator is not symmetric about the z-axis, in this paper, the ANSYS Maxwell software is employed to perform three-dimensional (3-D) finite-element analysis (FEA) of the magnetic circuit.

Before using FEA to optimize the structure, some design specifications of the MR actuator were specified. First, to achieve miniaturization, the rotor radius r of the actuator should not be greater than 10 mm. Second, the maximum output torque on all three axes should be greater than 0.3 N·m. According to (11) and (12), the MATLAB was used to calculate the maximum output torque of the MR actuator as a function of r and β_0 on the z-axis and x/y-axis. Fig. 8(a) and (b) shows the controllable output torque of the yawing motion and the pitching/rolling motion, respectively.

As can be seen from Fig. 8, when r is 10 mm, the maximum output torques of the z-axis and the x/y-axis are 0.3371 and 0.3054 N·m, respectively, which satisfy the design requirements. In addition, we have also specified some of the parameters in Fig. 4. For ease of manufacture and assembly, g is set to 0.3 mm [29], and both h_3 and r_b are set to 1 mm. Therefore, according to (1)–(6), the values of β_1, β_2, β_3, and β_4 can be calculated to be 5.57°, 67.2°, 5.75°, and 41.48°, respectively, and both h_2 and h_4 are 7.2 mm.

Next, the parameters that need to be optimized using FEA include bottom stator height h_1, bobbin height h and diameter d, support platform radius r_p, and coil turns N. The optimization goal of the magnetic circuit geometry is to saturate the magnetic flux density acting on the MR fluid and the yoke, which is 1 T for the MR fluid and 1.6 T for the yoke. The coil is made of enameled copper wire with a diameter of 0.3 mm, and the maximum input current is 1 A.

After several rounds of structural simulation analysis under given parameters, the optimized structural specifications can be
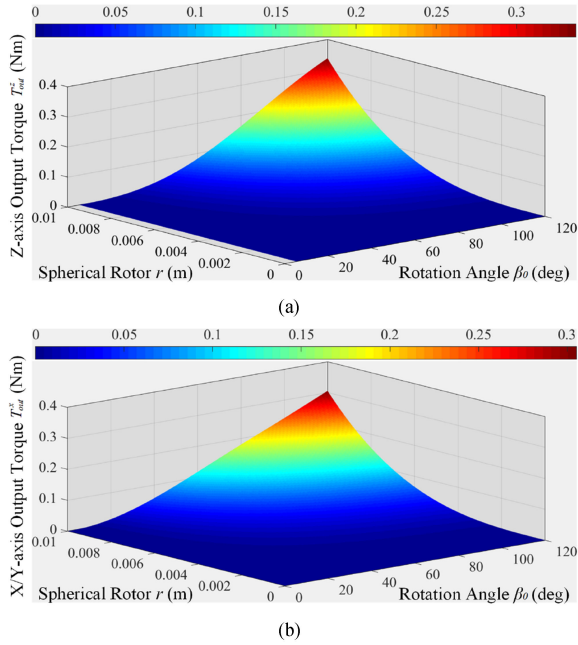
Fig. 8. Calculated controllable output torque. (a) Yawing motion. (b) Pitching/rolling motion.

TABLE I
STRUCTURAL AND FUNCTIONAL PARAMETERS OF THE MR ACTUATOR

| Parameter	Symbol	Value
Diameter of the MR actuator (mm)	D	43.8
Height of the MR actuator (mm)	H	33.5
Radius of the spherical rotor(mm)	r	10
Height of the bottom stator(mm)	h_1	5
Height of the spacer ring (mm)	h_3	1
Height of the bobbin(mm)	h	13.5
Diameter of the bobbin (mm)	d	6.8
Height of the spherical gap (mm)	g	0.3
Diameter of the enameled wire (mm)	d_c	0.3
Number of coil turns	N	180
Maximum coil current (A)	I_{max}	1
Maximum power consumption of eight coils (W)	P_{max}	8.56
Total mass (g)	m	173.3
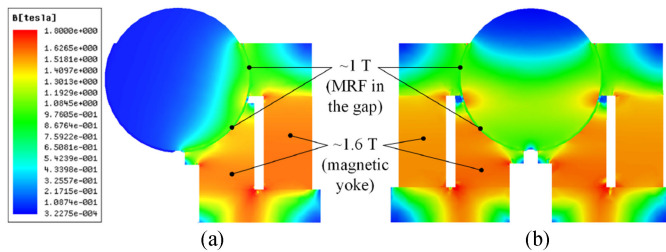
Fig. 9. Simulation results using FEA. (a) Single magnetic circuit unit activated by a current of 1 A (cross section). (b) Eight magnetic circuit units simultaneously activated by a current of 1 A (cross section).

obtained, as shown in Table I. Under the excitation of 1-A current, the simulation results of a single magnetic circuit are shown in Fig. 9(a), and the simulation results when eight magnetic circuits are simultaneously activated are shown in Fig. 9(b). From the above FEA results, it can be seen that under the action of the maximum magnetomotive force, the magnetic flux density applied to the MR fluid and the yoke reaches their respective
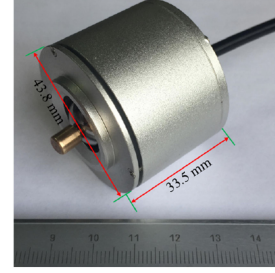

Fig. 10. Prototype of the proposed spherical MR actuator.

saturation values. The results show that the structural design of the actuator is reasonable, and the magnetic circuit design is effective.

Based on the structure dimensions obtained by FEA, we fabricated a spherical MR actuator prototype, as shown in Fig. 10. Its mass is 173.3 g, the maximum energy consumption is about 8.56 W, and the operating range is about ± 1 rad (pitching/rolling motion).

III. POSITION AND ATTITUDE TRACKING OF THE JOYSTICK

When interacting with a virtual environment, the user's operation information needs to be mapped to the virtual environment in real time in order to provide the user with realistic force feedback through a haptic device. There have been some studies using a combination of encoders and gimbal mechanisms [8], [22] or optical measurement systems [23] to detect the position and attitude of the joystick. However, the gimbal mechanisms inevitably increase the volume of the haptic device. Optical measurement systems require a structured environment and are susceptible to noise and shadowing [30].

In recent years, low-power, high-sensitivity, and small-sized microelectromechanical systems that are not limited by the measurement range and environmental conditions have been widely used for 3-D motion tracking and attitude capture [31]. In this paper, a commercial IMU called MPU6050 (InvenSense, USA) was integrated above the joystick to track the user's motion posture. Under certain conditions, both acceleration and angular rate can be used to calculate the attitude angle. On the one hand, when the joystick is stationary or moving at a constant speed, the average value of acceleration over a period of time is $(\bar{a}_x, \bar{a}_y, \bar{a}_z)$, and the attitude angle can be calculated as

$$\begin{pmatrix} \theta \\ \varphi \end{pmatrix} = \begin{pmatrix} \arctan(\frac{-\bar{a}_x}{\sqrt{\bar{a}_y^2 + \bar{a}_z^2}}) \\ \arctan(\frac{\bar{a}_y}{\bar{a}_z}) \end{pmatrix} \qquad (17)$$

where θ is the pitch angle and φ is the roll angle. However, in the motion environment where the acceleration suddenly changes, the attitude angle calculated by (17) will fail. On the other hand, in a short period of time, the attitude angle calculated by integrating the angular rate is credible. However, due to the accumulation of biases and drift errors, long-time integration will result in misalignment of the attitude angle. Therefore, in actual applications, it is usually necessary to fuse acceleration data and angular rate data to obtain accurate attitude information.

The Kalman filter is often used for filtering and data fusion. It can estimate the state of dynamic behavior based on the input

data of the IMU and ensure that the mean square error between the original state and the estimated state converges to the minimum [31]. The state equation of a linear discrete-time dynamic system can be expressed as

$$\begin{cases} x_k = Ax_{k-1} + Bu_{k-1} + w_k \\ z_k = Hx_k + v_k \end{cases} \tag{18}$$

where x_k, u_k, w_k, z_k, and v_k are the state vector, input vector, process noise vector, observation vector, and observation noise vector of the system at time $k(k = 1, 2, \ldots, n)$, respectively. A, B, and H are the state transition matrix, input weighting matrix, and observation matrix of the system, respectively. Using (18) as a rule base, the update of the Kalman filter state variables can be performed according to the following equations:

$$\hat{x}_k^- = A\hat{x}_{k-1}^- + Bu_{k-1} \tag{19}$$

$$P_k^- = AP_{k-1}^- A^T + Q \tag{20}$$

$$K_k = P_k^- H^T (HP_k^- H^T + R)^{-1} \tag{21}$$

$$\hat{x}_k = \hat{x}_k^- + K_k(z_k - H\hat{x}_k^-) \tag{22}$$

$$P_k = (1 - K_k H)P_k^- \tag{23}$$

where the symbols "^" and "−" indicate the current state estimation value and the state optimal value of the previous step, respectively. Q and R are the covariance matrix of the process and measurement noise, respectively. The posture of the device designed in this paper will not change drastically during work. Therefore, it is assumed that Q and R do not change with the system state. K is the Kalman gain, which can be calculated by (21). P is the estimate error covariance and is defined as

$$P_k = E[(x_k - \hat{x}_k)(x_k - \hat{x}_k)^T]. \tag{24}$$

Therefore, the current estimated state vector and the error covariance can be calculated by (22) and (23), respectively. In this algorithm, A, B, Q, H, and R are given as

$$A = \begin{bmatrix} 1 & -t_s \\ 0 & 1 \end{bmatrix}, \ B = \begin{bmatrix} t_s \\ 0 \end{bmatrix}$$

$$Q = \begin{bmatrix} 0.001 & 0 \\ 0 & 0.003 \end{bmatrix}, \ H = \begin{bmatrix} 1 & 0 \end{bmatrix}, \ R = 0.5 \tag{25}$$

where t_s is the system sampling time and is set to 0.01 s.

IV. EXPERIMENTS AND RESULTS

A. Torque Characteristics of the MR Actuator

To test the torque characteristics of the MR actuator, two experimental platforms were built. First, for the rotation of the joystick about the z-axis (yawing motion), the experimental platform is shown in Fig. 11(a). A Maxon dc motor RE-40 is connected to a 15:1 gearbox to produce drive torque and velocity. The motor uses an incremental encoder with 500 pulses per revolution to record the rotation angle of the shaft, and its rated torque is 2.655 N·m. The motor shaft is connected to a six-axis force/torque sensor (Mini 40, ATI Industrial Automation Inc., USA) via a coupler. The other end of the force/torque sensor is connected to the rotor of the MR actuator via a copper rod. Both the motor and the MR actuator are fixed on an aluminum base.
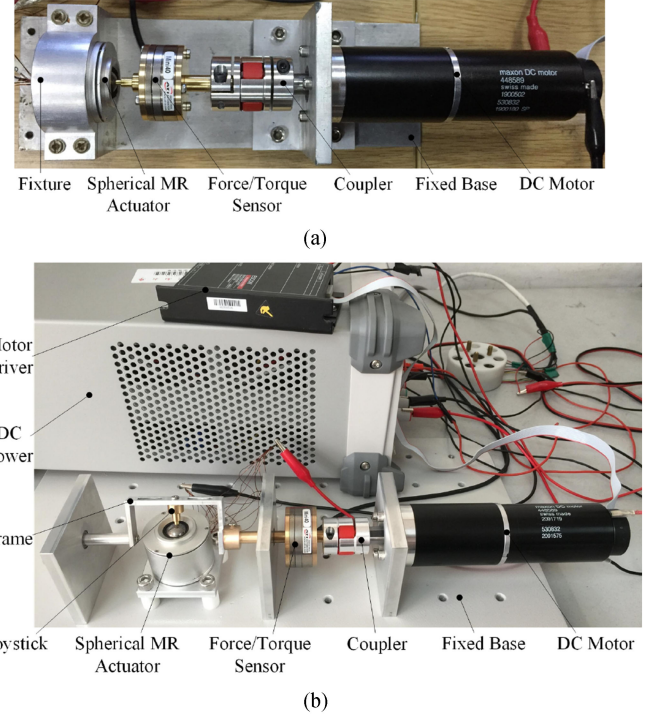

Fig. 11. Experimental platform. (a) Joystick rotation around the z-axis (yawing motion). (b) Joystick rotation around the x/y-axis (pitching/rolling motion).

All experimental devices are coaxially connected. The motor is controlled by a discrete servo controller with a sampling frequency of 10 kHz (ESCON 50/5, Maxon, Switzerland). The current applied to all the coils in the MR actuator is controlled by a customized multichannel constant current-source circuit. A data acquisition device (myDAQ, National Instruments, USA) records the output force/torque data of the MR actuator at a sampling rate of 1 kHz. Second, the experiment platform shown in Fig. 11(b) is used to measure the torque characteristics of the MR actuator when the joystick is rotated about the x/y-axis (pitching/rolling motion). The spherical actuator is fixed to the base. The center of the rotor is at the same level as the axis of the motor shaft. The upper part of the joystick is connected to the frame by a screw. The motor can drive the force/torque sensor, the frame, and the joystick to rotate together.

1) Z-Axis Torque Output Characteristics: The test platform of Fig. 11(a) was used to perform this test. During the experiment, the motor rotated at an angular speed of $\pi/2$ rad/s. For each control condition, three consecutive experiments were performed, and each test lasted 2–4 s. The average of three experimental results was recorded as the final result of this control condition. First, the motor rotated without applying current to the MR actuator. The measured initial OFF-state torque of the MR actuator caused by the viscosity of the MR fluid and the internal mechanical friction of the actuator was approximately 8.0 mN·m. Then, the torque–current relationship of the MR actuator was tested. The current applied to the coil increased from 0 to 1 A in a step of 0.1 A and then decreased to 0 A in the same step. When a single coil is energized, the torque–current relationship of the MR actuator is shown in Fig. 12(a).
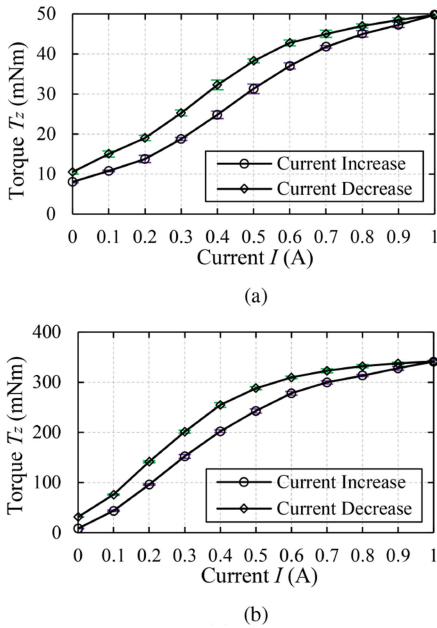
Fig. 12. Torque–current relationship of the MR actuator. (a) Single coil is energized. (b) Eight coils are energized.
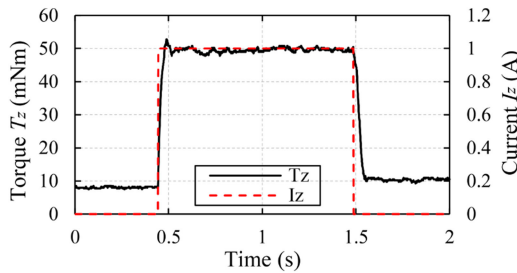

Fig. 13. Transient response of the MR actuator. T_z is the output torque of the z-axis, and I_z is the excitation current acting on a single coil.

Using the same experimental procedure, the torque–current relationship of the MR actuator when the eight coils are energized simultaneously is shown in Fig. 12(b).

The experimental results show that under the excitation of 1-A current, the single coil produces a maximum output torque of 49.75 mN·m. The maximum output torque available when the MR actuator rotates about the z-axis is 341.25 mN·m. Taking into account the initial OFF-state torque that has been measured, the dynamic range of the MR actuator can be calculated as 32.6 dB. Since the ferromagnetic material in the magnetic circuit is magnetized by the magnetic field, obvious hysteresis can be observed from Fig. 12. The maximum torque deviation caused by hysteresis at both control conditions occurred at the current of 0.4 A, which was 7.5 and 52.25 mN·m, respectively. Therefore, the hysteresis effect has a great influence on the output torque. To eliminate the remanence, the control circuit applies a small reverse current to the coil after the excitation current is reduced to zero.

2) Transient Response: To investigate the time constant of the MR actuator, the experimental platform of Fig. 11(a) was used to test its transient response characteristics. Fig. 13 shows the output torque when a single coil is energized under the action of a step current. From the results, it can be seen that the MR
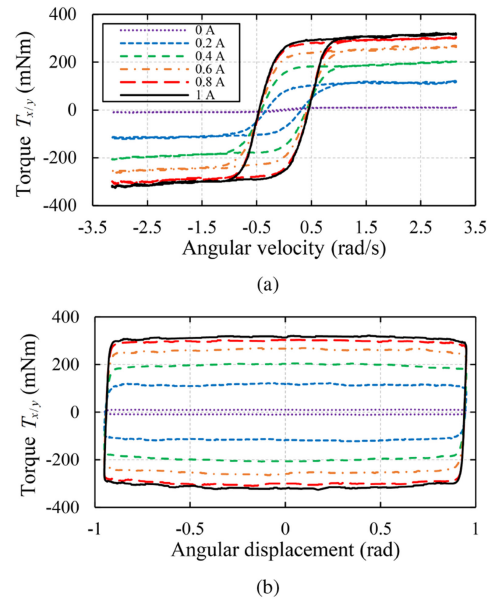

Fig. 14. Test results for rotation around the x/y-axis at multiple current levels. (a) Torque–angular velocity curve. (b) Torque–angular displacement curve.

actuator exhibits a similar dynamic behavior as the first-order linear system. The step rise and the fall times are 25.28 and 37.92 ms, respectively.

3) X/Y-Axis Force Output Characteristics: In the case of applying the same magnitude and direction of current to all coils, we used the experimental platform shown in Fig. 11(b) to test the torque–angular velocity relationship and torque–angular displacement relationship of the actuator when the joystick was rotated about the x/y-axis. During the experiment, a sinusoidal excitation having a frequency of 0.5 Hz and an amplitude of 0.95 rad was applied to the motor to drive the joystick to swing left and right. The test results at multiple current levels are shown in Fig. 14.

Fig. 14 shows that the maximum torque of the actuator about the x/y-axis is 312 mN·m. However, when all magnetic circuits are activated, the MR actuator provides the same magnitude of force/torque for the joystick's nutation in all directions. To investigate the ability of the MR actuator to output torque that varies with the direction of operation, we also used Fig. 11(b) to measure the torque characteristics of the MR actuator when a single magnetic circuit was activated. First, adjust the attitude of the actuator in Fig. 11(b) according to the coordinate system of Fig. 3(b), so that the motor can drive the joystick to move around the y-axis in the xoz plane of Fig. 3(b). The test used a current of 1 A to activate the magnetic circuit 1 and still applied a sinusoidal excitation with a frequency of 0.5 Hz and an amplitude of 0.95 rad to the motor. Next, the body of the actuator was rotated from 0 to 1.5708 rad in steps of 0.2618 rad around the z-axis. Five tests were performed for each attitude of the actuator. The average value of the output torque of the actuator in each attitude is shown in Fig. 15. As can be seen from Fig. 15, when a single magnetic circuit is activated, the output torque of the actuator about the x/y-axis will change with the direction of the nutation.
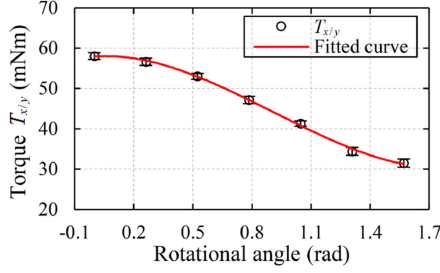
Fig. 15. Output torque of the MR actuator on the x/y-axis as the nutating direction of the joystick is rotated relative to the activated magnetic circuit.
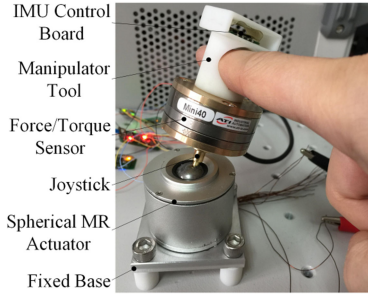

Fig. 16. Experimental setup for measuring the output force of the MR actuator when the joystick is rotated about the *x/y*-axis.

B. Performance Evaluation

1) Virtual Softness Display: This test evaluated the force feedback performance of the MR actuator in a single direction by displaying the softness of a virtual object. We fixed an MPU6050-based IMU control board to the upper part of the manipulator tool in Fig. 16 to detect the attitude and position of the joystick. The torque arm of the actuator on the *x/y*-axis is 25.57 mm. In order to ensure that the MR actuator outputted correct force with the change of the interaction direction, the coordinate system of Fig. 3(b) should be consistent with the coordinate system of the IMU control board. The spring–mass model was used to create a virtual plane, and the joystick was replaced with a HIP in the virtual environment. Referring to Fig. 3(b), the position of the virtual plane coincides with the xoz plane. When the HIP penetrates the virtual plane, the virtual interaction force F_v can be calculated by the following equation:

$$F_v = k_v x + b\dot{x}, \ x \geq 0 \quad (26)$$

where x is the penetration depth, and k_v and b are the stiffness and damping coefficients of the virtual plane, respectively. k_v is set to 4 N/rad, and b is 0.1 N·s/rad.

During the experiment, the joystick was placed in the yoz plane and coincided with the oz-direction. Then, the joystick penetrated the virtual plane in the positive direction of the oy. During the operation of the joystick, the position and posture information recorded by the IMU was transmitted to the virtual environment. The virtual model calculated the virtual interaction force according to (26) and sent the current control signal to the control circuit through Bluetooth. Then, the MR actuator output
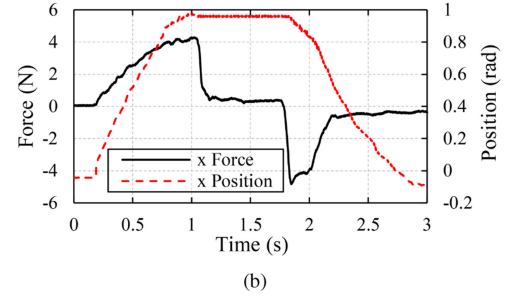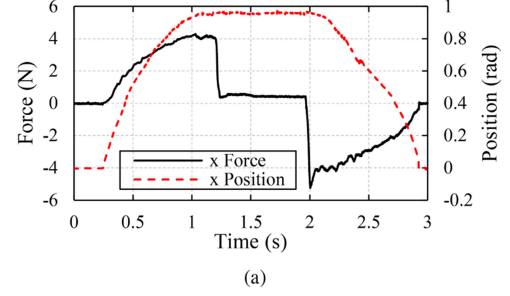

(a)

(b)

Fig. 17. Softness display results. (a) Sticky feeling is felt during the whole process of pulling the HIP back from the virtual plane. (b) Reduce the effect of sticky feeling on interaction by combining position information.

a passive force. The results of the experimental recording are shown in Fig. 17(a).

In Fig. 17(a), the output force of the MR actuator increases nonlinearly with increasing penetration depth. After the HIP reaches the maximum penetration depth, the user stops moving. However, magnetic circuits 3 and 7 were still activated. Therefore, the user needs to exert more force to pull the HIP back from the virtual plane, and the user will have a sticky feeling during the whole process of pulling back the HIP, which will lead to an unrealistic interaction experience.

To reduce the effect of the sticky feeling on interactions, the real-time attitude data collected by the IMU were used to guide the force output of the MR actuator. That is, when the user pulls the HIP back from the virtual plane, if the system detects that the movement angle of the joystick in the negative direction of the oy is greater than 0.1 rad, the current is no longer input to magnetic circuits 3 and 7, and they are reversely demagnetized at the same time. The experimental results are shown in Fig. 17(b). From the results, it can be seen that although the sticky feeling cannot be completely eliminated, the MR actuator still effectively reduces the duration of the sticking effect by combining with the inexpensive IMU, which helps to enhance the realism of the multi-DOF interaction.

2) Virtual Friction Display: This experiment used the same experimental setup as the virtual softness display to investigate the ability of the MR actuator in displaying the Coulomb friction of the virtual surface. For ease of fulfillment and computation, the Karnopp friction model was employed in this experiment [32]. This model uses a velocity threshold to divide the friction into static and dynamic states, which can be expressed as [33]

$$F_f = \begin{cases} F_d \cdot \text{sgn}(v_K), & |v_K| > \Delta v \\ \min(F_s, F_a), & |v_K| \leq \Delta v \end{cases} \quad (27)$$
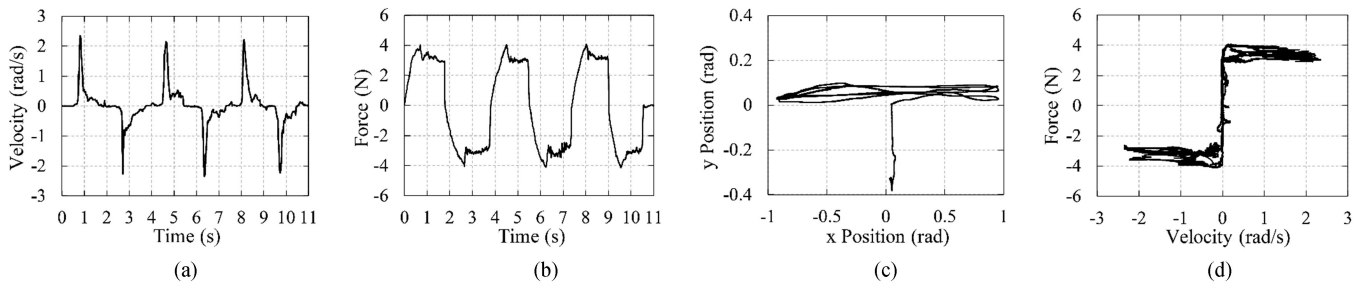
Fig. 18.   Coulomb friction displayed by the prototype MR actuator. (a) Velocity as a function of time. (b) Actual force. (c) The trajectory measured by the IMU. (d) Force versus velocity.

where F_f, F_d, F_s, F_a, Δv, and v_K denote the frictional force, dynamic friction, static friction, applied force, velocity threshold, and kinematic velocity, respectively. When the kinematic velocity is less than Δv, the system is considered in the static state. At this time, the small movement of the system away from the stuck position can be simulated by a virtual spring with stiffness k_K, and the applied force F_a is calculated by Hooke's law, which can be expressed as

$$F_a = -k_K(x - x_{\text{stuck}}). \tag{28}$$

When F_a increases beyond the maximum static friction, the system switches to the dynamic state. Once the kinematic velocity is lower than Δv, the system transitions back to the static state again. In this experiment, the velocity threshold was set to 0.15 rad/s, the Karnopp stiffness k_K was 100 N/rad, the static friction F_s was 4 N, and the dynamic friction F_d was 3 N. During the experiment, the HIP penetrated the virtual surface in the positive direction of the oy and then nutation around the y-axis after contact. Fig. 18 shows the results of the Coulomb friction displayed by the MR actuator. From the results, it can be seen that the MR actuator can accurately display the Coulomb friction of the virtual surface. Due to the passive nature, the MR actuator performs more stable than active actuators in simulating discontinuous forces [33].

V. CONCLUSION

This paper presents a small multidirectional controlled three-DOF spherical MR actuator for haptic applications. The actuator integrates eight independent magnetic circuit units for force/torque control in multiple DOFs and directions. This design mainly used to solve the problem that the traditional semiactive spherical actuator locks all DOFs after being activated and outputs a fixed magnitude of force/torque in all directions of motion. First, we investigated the principles of designing the spherical MR actuator through the torque model and magnetic field analysis. The structural parameters and magnetic field distribution were optimized by FEA. We then conducted two groups of experiments to evaluate the effectiveness of the proposed MR actuator. Tests on the torque characteristics of the MR actuator show that the maximum output torque of the MR actuator on the z-axis and x/y-axis meets the design requirements. Fig. 15 shows that when a single magnetic circuit is activated, the actuator outputs variable torques in different directions. This is why when the MR actuator is used to perform a virtual wall

collision operation, the user can still perceive the friction features by sliding on the surface of the virtual wall. In the softness display experiment, the combination of the MR actuator and an inexpensive IMU effectively reduces the influence of the "stuck in the wall" characteristic of the semiactive actuator on the user. The display of Coulomb friction also shows that the combination with the IMU helps the MR actuator to better complete the virtual interaction operation.

Since the force/torque information in any interactive direction and DOF can be displayed by any combination of eight magnetic circuits, the actuator proposed in this paper is more suitable for interaction with complex virtual environments, and more in line with the needs of multi-DOF and multidirectional HCI. Moreover, the actuator can be used as a key component of a haptic device, such as a wearable device, an exoskeleton device, a portable HCI device, and a rehabilitation medical device, for reducing the structural complexity, volume, and weight of these devices, and enhancing the realism of the haptic interaction.

REFERENCES

[1] B. Hannaford and A. M. Okamura, "Haptics," in *Springer Handbook of Robotics*. New York, NY, USA: Springer, 2016, pp. 1063–1084.
[2] G. C. Burdea, *Force and Touch Feedback for Virtual Reality*. New York, NY, USA: Wiley-Interscience, 1996.
[3] V. Hayward, O. R. Astley, M. Cruz-Hernandez, D. Grant, and G. Robles-De-La-Torre, "Haptic interfaces and devices," *Sens. Rev.*, vol. 24, no. 1, pp. 16–29, 2004.
[4] T. R. Coles, D. Meglan, and N. W. John, "The role of haptics in medical training simulators: A survey of the state of the art," *IEEE Trans. Haptics*, vol. 4, no. 1, pp. 51–66, Jan.–Mar. 2011.
[5] J. An and D. S. Kwon, "Haptic experimentation on a hybrid active/passive force feedback device," in *Proc. IEEE Int. Conf. Robot. Autom.*, 2002, vol. 4, pp. 4217–4222.
[6] T. H. Massie and J. K. Salisbury, "The phantom haptic interface: A device for probing virtual objects," *ASME Dyn. Syst. Control Div.*, vol. 55, pp. 295–300, 1994.
[7] G. Zhang, J. Furusho, and M. Sakaguchi, "Vibration suppression control of robot arms using a homogeneous-type electrorheological fluid," *IEEE/ASME Trans. Mechatronics*, vol. 5, no. 3, pp. 302–309, Sep. 2000.
[8] W. H. Li, B. Liu, P. B. Kosasih, and X. Z. Zhang, "A 2-DOF MR actuator joystick for virtual reality applications," *Sens. Actuators A, Phys.*, vol. 137, no. 2, pp. 308–320, 2007.
[9] J. Blake and H. B. Gurocak, "Haptic glove with MR brakes for virtual reality," *IEEE/ASME Trans. Mechatronics*, vol. 14, no. 5, pp. 606–615, Oct. 2009.
[10] D. Case, B. Taheri, and E. Richer, "Dynamical modeling and experimental study of a small-scale magnetorheological damper," *IEEE/ASME Trans. Mechatronics*, vol. 19, no. 3, pp. 1015–1024, Jun. 2014.
[11] D. Chen, A. Song, L. Tian, Y. Yu, and L. Zhu, "MH-Pen: A pen-type multi-mode haptic interface for touch screens interaction," *IEEE Trans. Haptics*, vol. 11, no. 4, pp. 555–567, Oct.–Dec. 2018.

[12] J. Arata, H. Kondo, N. Ikedo, and H. Fujimoto, "Haptic device using a newly developed redundant parallel mechanism," *IEEE Trans. Robot.*, vol. 27, no. 2, pp. 201–214, Apr. 2011.

[13] N. Najmaei, A. Asadian, M. R. Kermani, and R. V. Patel, "Design and performance evaluation of a prototype MRF-based haptic interface for medical applications," *IEEE/ASME Trans. Mechatronics*, vol. 21, no. 1, pp. 110–121, Feb. 2016.

[14] J. Viau, P. Chouinard, J. P. L. Bigué, G. Julió, F. Michaud, and J. S. Plante, "Tendon-driven manipulator actuated by magnetorheological clutches exhibiting both high-power and soft motion capabilities," *IEEE/ASME Trans. Mechatronics*, vol. 22, no. 1, pp. 561–571, Feb. 2017.

[15] S. M. Lee and H. Son, "Multidegree-of-freedom motion platform based on spherical wheels," *IEEE/ASME Trans. Mechatronics*, vol. 22, no. 5, pp. 2121–2129, Oct. 2017.

[16] L. Yan, I. M. Chen, C. K. Lim, G. Yang, and K. M. Lee, *Design, Modeling and Experiments of 3-DOF Electromagnetic Spherical Actuators* (Mechanisms and Machine Science). New York, NY, USA: Springer, 2011.

[17] L. Rossini, O. Chételat, E. Onillon, and Y. Perriard, "Force and torque analytical models of a reaction sphere actuator based on spherical harmonic rotation and decomposition," *IEEE/ASME Trans. Mechatronics*, vol. 18, no. 3, pp. 1006–1018, Jun. 2013.

[18] N. Kasashima, K. Ashida, T. Yano, A. Gofuku, and M. Shibata, "Torque control method of an electromagnetic spherical motor using torque map," *IEEE/ASME Trans. Mechatronics*, vol. 21, no. 4, pp. 2050–2060, Aug. 2016.

[19] J. D. Carlson, D. M. Catanzarite, and K. A. S. Clair, "Commercial magneto-rheological fluid devices," *Int. J. Modern Phys. B*, vol. 10, pp. 2857–2865, 1996.

[20] H. Bose and H. J. Berkemeier, "Haptic device working with an electrorheological fluid," *J. Intell. Mater. Syst. Struct.*, vol. 10, no. 9, pp. 714–717, 1999.

[21] Y. M. Han and S. B. Choi, "Force-feedback control of a spherical haptic device featuring an electrorheological fluid," *Smart Mater. Struct.*, vol. 15, no. 5, pp. 1438–1446, 2006.

[22] J. S. Oh, Y. M. Han, S. R. Lee, and S. B. Choi, "A 4-DOF haptic master using ER fluid for minimally invasive surgery system application," *Smart Mater. Struct.*, vol. 22, 2013, Art. no. 045004.

[23] D. Senkal and H. Gurocak, "Spherical brake with MR fluid as multi degree of freedom actuator for haptics," *J. Intell. Mater. Syst. Struct.*, vol. 20, no. 18, pp. 2149–2160, 2009.

[24] M. J. Telleria, R. M. Panas, and M. L. Culpepper, "MR fluid activated spherical joint for precision orientation control," in *Proc. 24th Amer. Soc. Precis. Eng. Annu. Meeting*, 2009.

[25] J. An and D. S. Kwon, "Five-bar linkage haptic device with DC motors and MR brakes," *J. Intell. Mater. Syst. Struct.*, vol. 20, no. 1, pp. 97–107, 2009.

[26] M. R. Jolly, J. W. Bender, and J. D. Carlson, "Properties and applications of commercial magnetorheological fluids," *J. Intell. Mater. Syst. Struct.*, vol. 10, no. 1, pp. 5–13, 1999.

[27] Q. H. Nguyen, S. B. Choi, and N. M. Wereley, "Optimal design of magnetorheological valves via a finite element method considering control energy and a time constant," *Smart Mater. Struct.*, vol. 17, no. 2, 2008, Art. no. 025024.

[28] Y. J. Nam, Y. J. Moon, and M. K. Park, "Performance improvement of a rotary MR fluid actuator based on electromagnetic design," *J. Intell. Mater. Syst. Struct.*, vol. 19, no. 6, pp. 695–705, 2008.

[29] J. H. Yoo and N. M. Wereley, "Design of a high-efficiency magnetorheological valve," *J. Intell. Mater. Syst. Struct.*, vol. 13, no. 10, pp. 679–685, 2002.

[30] T. L. Baldi, S. Scheggi, L. Meli, M. Mohammadi, and D. Prattichizzo, "GESTO: A glove for enhanced sensing and touching based on inertial and magnetic sensors for hand tracking and cutaneous feedback," *IEEE Trans. Human–Mach. Syst.*, vol. 47, no. 6, pp. 1066–1076, Dec. 2017.

[31] X. Yun and E. R. Bachmann, "Design, implementation, and experimental results of a quaternion-based Kalman filter for human body motion tracking," *IEEE Trans. Robot.*, vol. 22, no. 6, pp. 1216–1227, Dec. 2006.

[32] D. Karnopp, "Computer simulation of stick-slip friction in mechanical dynamic systems," *J. Dyn. Syst. Meas. Control*, vol. 107, no. 1, pp. 100–103, 1985.

[33] J. An and D. S. Kwon, "Stability and performance of haptic interfaces with active/passive actuators—Theory and experiments," *Int. J. Robot. Res.*, vol. 25, no. 11, pp. 1121–1136, 2006.

Dapeng Chen (S'18) received the B.S. degree in electrical engineering and automation from the Anhui University of Science and Technology, Huainan, China, in 2011. He is currently working toward the Ph.D. degree in instrument science and technology with the School of Instrument Science and Engineering, Southeast University, Nanjing, China.

He was a Visiting Scholar with the Intelligent, Multimedia, and Interactive Systems Lab, University of North Carolina at Charlotte, Charlotte, from 2016 to 2017. His research interests include haptic display, haptic device, human–computer interaction, and novel actuator design with smart materials.

Aiguo Song (M'98–SM'11) received the B.S. degree in automatic control and the M.S. degree in measurement and control from the Nanjing University of Aeronautics and Astronautics, Nanjing, China, in 1990 and 1993, respectively, and the Ph.D. degree in measurement and control from Southeast University, Nanjing, in 1996.

He is currently the Dean, a Professor, and a Doctoral Supervisor with the School of Instrument Science and Engineering, Southeast University, and also the Director of the Robot Sensing and Control Technology Laboratory. His research interests include haptic display, robot tactile sensor, rehabilitation engineering, and robotic teleoperation technology.

Dr. Song was a recipient of the National Science Fund for Distinguished Young Scholars in 2013 and the Second Prize of the National Technology Invention of China in 2017.

Lei Tian received the B.S. degree in electronic information engineering from Jilin University, Changchun, China, in 2003, and the Ph.D. degree in instrumentation science and technology from Southeast University, Nanjing, China, in 2016.

She is currently a Lecturer with the School of Automation, Nanjing Institute of Technology, Nanjing. Her research interests include haptic rendering, computer vision, and human–computer interaction.

Qiangqiang Ouyang received the B.S. and M.S. degrees in electrical and information engineering from the Anhui University of Technology, Ma'anshan, China, in 2012 and 2016, respectively. He is currently working toward the Ph.D. degree in instrument science and technology with the School of Instrument Science and Engineering, Southeast University, Nanjing, China.

He is also a Visiting Student with the David Geffen School of Medicine, University of California at Los Angeles, Los Angeles, CA, USA. His research interests include modeling and application of tactile illusion.

Pengwen Xiong received the B.S. degree from the North University of China, Taiyuan, China, in 2009, and the Ph.D. degree in instrumentation science and technology from Southeast University, Nanjing, China, in 2015.

He was a Visiting Scholar with the Laboratory for Computational Sensing and Robotics, Johns Hopkins University, from 2013 to 2014. He is currently an Associate Professor with the School of Information Engineering, Nanchang University, Nanchang, China. His research interests include human–robot interaction and robotic sensing and control.